Molecules during Stellar Formation and Death

Li, X.

Chapter 4

New chemistry in O-rich AGB stars

Abstract.
Context. Thanks to the advent of *Herschel* and ALMA, new high-quality observations of molecules present in the circumstellar envelopes of AGB stars are being reported, which reveal large differences to existing chemical models. New molecular data and more comprehensive models of the chemistry in circumstellar envelopes are now available.
Aims. The aims are to determine and study the important formation and destruction pathways in the envelopes of O-rich AGB stars, and to provide more reliable predictions of abundances, column densities, and radial distributions for potentially-detectable species, with physical conditions applicable to the envelope surrounding IK Tau.
Methods. We use a large gas-phase chemical model of an AGB envelope including the effects of CO and N_2 self-shielding in a spherical geometry and a newly-compiled list of inner-CSE parent species derived from detailed modelling and observations. We trace the dominant chemistry in the expanding envelope and investigate the chemistry as a probe for the physics of the AGB phase by studying variations of abundances with mass loss rates and expansion velocities.
Results. We find a pattern of daughter molecules forming from the photodissociation products of parent species, with contributions from ion-neutral abstraction and dissociative recombination. The chemistry in the outer zones differs from that in traditional PDRs in that photoionization of daughter species plays a significant role. With the proper treatment of self-shielding, the N $\rightarrow N_2$ and $C^+ \rightarrow$ CO transitions are shifted outward by factors of 7 and 2 compared with earlier models, respectively. An upper limit on the abundance of CH_4 as a parent species of ($\lesssim 2.5 \times 10^{-6}$ with respect to H_2) is found for IK Tau, and several potentially-observable molecules with relatively simple chemical links to other parent species are determined. The assumed stellar mass-loss rate, in particular, has an impact on the calculated abundances of cations and the peak-abundance radius of both cations and neutrals: as the mass-loss rate increases, the peak abundance of cations generally decrease and the peak-abundance radius of all species moves outwards. The effects of varying the envelope expansion velocity and cosmic-ray ionisation rate are not as significant.

X. Li, T. J. Millar, A. N. Heays, C. Walsh, E. F. van Dishoeck, and I. Cherchneff
Submitted to *A&A* (2015).

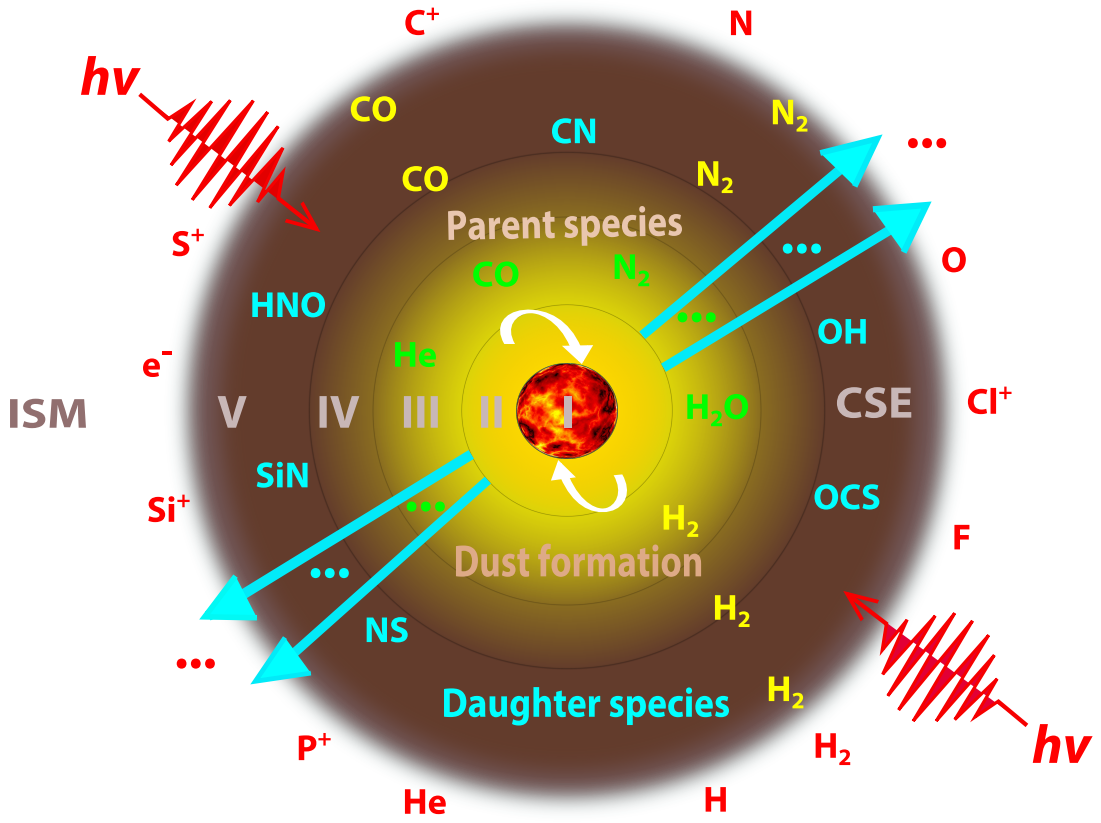

Figure 4.1 — Schematic structure of the CSE for an O-rich AGB star, which is divided into 6 regions for modelling purposes. (I): a degenerate C/O core and He/H burning shell, (II): a convective atmosphere, (III): a shocked inner wind where some parent species (mainly H_2O, CO, and SiO) are formed, (IV): an intermediate expanding envelope where gas-phase chemistry may play a role, (V): an outer CSE where daughter species are formed primarily by photodissociation, (VI): the interstellar medium (ISM). This study focusses on the outer CSE where chemistry is mainly driven by the photodissociation and photoionization of molecules.

4.1 Introduction

The asymptotic giant branch (AGB) phase occurs when stars from 0.8 to 8 $M_\odot$ are undergoing their last nuclear burning (Iben & Renzini 1983; Herwig 2005) and is a particularly interesting environment in which to study molecule formation and destruction. As shown in Fig. 4.1, the distribution and chemistry of species in the outer expanding circumstellar envelopes (CSEs), namely "daughter" species, are driven by hot (1000 – 2000 K) and shocked processes in the inner CSE where "parent" species are formed.

There are three types of AGB stars: C-rich (C/O $>$ 1), S-type (C/O $\approx$ 1), and O-rich (M-type, C/O $<$ 1). The largest variety of molecules is found in the CSE of C-rich stars, from simple CO to large polycyclic aromatic hydrocarbons (PAHs, e.g., Boersma et al. 2006; Cherchneff 2012). The best-investigated AGB star, both observationally and theoretically, is the nearest C-rich star, IRC +10216 (e.g., Millar et al. 2000; Cernicharo et al. 2000; Woods et al. 2003; Cordiner & Millar 2009; Decin et al. 2010; De Beck et al. 2012; Cherchneff 2012; McElroy et al. 2013; Li et al. 2014). To date, more than 44% of the

180 identified species in the interstellar medium (ISM) or CSEs[a] have been detected in this star, with some being first detections in astrophysical environments, e.g., the cyanide anion CN^- (Agúndez et al. 2010b), and FeCN (Zack et al. 2011). A relatively small, but increasing, number of investigations have been made into S-type AGB stars (e.g., Ramstedt et al. 2006, 2009, 2011; Schöier et al. 2011; Danilovich et al. 2014), in which the central stars are undergoing evolution from an O-rich to a C-rich phase. During this transition, mixed chemistry may occur, especially when the O-rich material is stored in a stable disk around the central star, and features of both C-rich and O-rich chemistry may appear (Willems & de Jong 1986; Szczerba et al. 2007). This interesting dual chemistry may continue to post-AGB stars, and even proto-planetary nebulae (pPNe, see Gielen et al. 2011,and references therein).

Significant progress in the investigation of O-rich circumstellar envelopes has been driven by new telescopes (Ziurys et al. 2007; Tenenbaum et al. 2010; Decin 2012), especially the Heterodyne Instrument for the Far-Infrared (HIFI) aboard the *Herschel Space Observatory* (Pilbratt et al. 2010), which provided velocity-resolved spectra at far-infrared wavelengths that are not accessible from the ground. Several small molecules have been identified in O-rich evolved stars, for instance, CO, H_2O, HCN, HNC, CN, OH, NO, SiS, and SiO, (e.g., Cho & Ukita 1998; Ziurys 2006; Schöier et al. 2007; Ziurys et al. 2009; Maercker et al. 2009; Decin et al. 2010a). In addition, some O-bearing inorganic species, e.g., AlO and AlOH, have been identified in the supergiant VY Canis Majoris (Tenenbaum & Ziurys 2010). Moreover, emission from PAHs and fullerenes C_{60} have also surprisingly been found in O-rich binary post-AGB sources (Gielen et al. 2011). All of these studies clearly show a rich inventory of molecules due to complex chemistry in the CSEs around O-rich central stars. The Atacama Large Millimeter/submillimeter Array (ALMA) is now starting to provide very sensitive, spatially resolved images of AGB envelopes as evidenced by the resolved shells of the AGB star R Sculptoris by Maercker et al. (2012). It is therefore timely to revisit the chemistry in these sources with an updated chemistry network.

In this work, we mainly focus on the well-observed O-rich AGB star, IK Tau. This source has a large mass-loss rate of $\sim 4.5 \times 10^{-6}$ $M_\odot$ yr^{-1} (De Beck et al. 2010) in a wind that expands at a terminal velocity of 24 km s^{-1} (Justtanont et al. 2012). Note that these values are model dependent and may be different from those deduced from other observations (e.g., Maercker et al. 2008; Decin et al. 2010a). A few 'parent' species (i.e., those formed close to the stellar photosphere) have been detected in the inner CSE of IK Tau in recent years, for instance, CO, HCN, CS, SiS, SiO, SO, and SO_2 (Decin et al. 2010a; Kim et al. 2010), H_2O (Decin et al. 2010b), NH_3 (Menten et al. 2010), PN and PO (De Beck et al. 2013). Schöier et al. (2013) conducted a survey of HCN in a sample of 69 stars which included all three types of AGB stars, including IK Tau, and concluded that the HCN abundances in C-rich AGB stars are, on average, around two orders of magnitude higher than those in O-rich stars. Fractional abundances of only two daughter species have been deduced from observations of IK Tau, CN (Decin et al. 2010a; Kim et al. 2010) and HCO^+ (Pulliam et al. 2011). OH emission was identified but not quantified (Polehampton et al. 2010). In addition, thermal CO and SiO polarization has

[a] `http://www.astro.uni-koeln.de/cdms/molecules/`

been mapped for IK Tau to study the orientation of its magnetic field (Vlemmings et al. 2012).

Theoretically, Willacy & Millar (1997) built a model specifically for O-rich CSEs and discussed the chemistry of daughter species in four sources: R Dor, TX Cam, OH231.8 +4.2, and IK Tau. At that time, only limited observational data and a restricted chemical network were available, therefore, some assumptions made in that work have since been discounted, e.g., CH_4 was assumed to be a parent species but the observations by Marvel (2005) provided no evidence for CH_4 based on sensitive searches for the chemically related CH_3OH and C_2H molecules. Agúndez et al. (2010a) employed an improved model to investigate the chemistry in both O-rich and C-rich AGB stars, and suggested that the model predictions could be altered by taking into account a clumpy structure for the CSE, even with a simple approach. An improved list of parent species from observations was employed, but some parent species, e.g., NH_3 and HCN, had not yet been observed at that time, and therefore were not included as parents. The assumed abundances of parent species is very important in the simulation of outer CSE chemistry, because these species trigger and drive the chemistry of daughter species. Previously, local thermodynamical equilibrium (LTE) predictions were used to determine the parent species. However, predictions from shock-induced non-LTE calculations (Duari et al. 1999; Cherchneff 2006) significantly differ from these, e.g., Cherchneff (2006) concluded that four species, CO, SiO, HCN, and CS, can exist in both C-rich and O-rich stars. The conclusion was later confirmed through observations (Decin et al. 2008).

In previous work we developed a model that, for the first time, accurately treated the photodissociation of two significant parent species, CO and N_2, in the CSE of a C-rich star, IRC +10216 (Li et al. 2014). Here, we adapt this model to study the chemistry of O-rich AGB stars. The recent progress of both observations and models makes a detailed and more reliable simulation possible. The chemistry of a large number of potentially observable species, including C-, N-, O-, Si-, S-, P-, Cl-, and F-bearing species, are discussed.

This chapter is organised as follows: the CSE model and improvements in this study are described in Sect. 4.2, followed by the results and discussion in Sect. 4.3, and conclusions, in Sect. 4.4. A general investigation of the effects of varying the mass-loss rate and expansion velocity on the distributions of species is included in the Appendix.

4.2 Improvements in our models

4.2.1 Improvements in the model

The CSE model assumes that the gas expands in a smoothly expanding envelope with a constant mass-loss rate and velocity. The main assumptions of the model and envelope parameters of the O-rich AGB star, IK Tau, are listed in Table 4.1. More details about the CSE model can be found in McElroy et al. (2013), Millar et al. (2000), and Cordiner & Millar (2009). The kinetic temperature of the gas, T, number density of molecular hydrogen, $n(H_2)$, and visual extinction, A_V, are shown in Fig. 4.2. The density follows a r^{-2} behaviour dictated by conservation of mass and the temperature structure

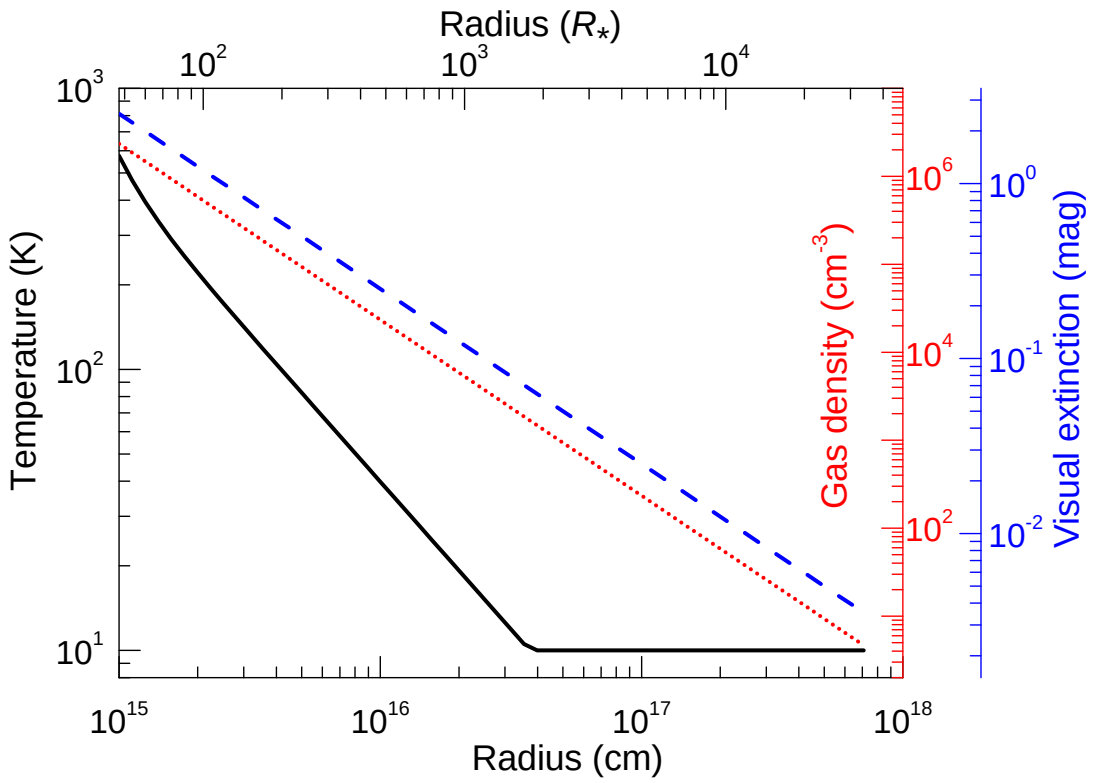

Figure 4.2 — Gas density, visual extinction, and gas temperature as a function of radius for the CSE of IK Tau from the center of the star towards the outside of the envelope. The radius is given in units of cm and stellar radii, R_*.

Table 4.1 — Envelope parameters and assumptions for IK Tau in our fiducial model.

1.	Shape	Spherical
2.	Mass-loss rate	4.5(-6) $M_\odot$ yr^{-1} (De Beck et al. 2010)
3.	Envelope expansion velocity	24 km s^{-1} (Justtanont et al. 2012)
4.	Stellar radius, R_*	2.1×10^{13} cm (Duari et al. 1999)
5.	Inner radius of CSE	10^{15} cm
6.	External radiation field	Draine (1978) field, isotropic incidence
7.	Grain surface reactions	Ignored
8.	Gas density distribution	Falls as r^{-2}, where r is the radius
9.	Chemical evolution	Kinetic equations solved as a function of radius
10.	H_2	Fully self-shielded, no photodissociation
11.	Parent species	See Table 4.2
12.	T, A_V, and gas density	See Fig. 4.2
13.	Cosmic-ray ionisation rate scaling factor	1

is calculated according to the following relation enforcing a 10 K lower limit

$$T(r) = \max\left(100\,(r/r_i)^{-0.79}, 10\right), \tag{4.1}$$

where r_i is the inner radius of our model. Extinction of the incident radiation is derived assuming purely absorbing grains and using standard values for the interstellar gas-to-dust ratio and extinction curve (Bohlin et al. 1978; Savage & Mathis 1979).

The chemistry of daughter species in the outer CSE is dominated by photodissociation. FUV photons from all directions of the interstellar medium are considered to contribute to the photodissociation rate of each species. IK Tau is of spectral type M6 with an effective temperature ≈ 2100 K (see, e.g, Duari et al. 1999); hence, the UV flux arising from the star itself is negligible. The model is assumed to be fully spherically-symmetric (SS model, Li et al. 2014) and accurately calculates the shielding effects of molecules in an isotropic interstellar radiation field.

The fifth release of the UMIST Database for Astrochemistry (UDfA, McElroy et al. 2013), hereafter RATE12, which contains 6173 gas-phase reactions involving 467 species, is further updated with a few new rate coefficients for the most significant nitrogen reactions (Wakelam et al. 2013), and adopted in all of the calculations. Very minor differences (within 2%) of the predicted peak abundances of the species are found when using these new rate coefficients, compared with those using RATE12.

The treatment of N_2 and CO photodissociation is the same as that described in our previous work (Li et al. 2014). Accurate photodissociation rates and shielding functions of N_2 (Li et al. 2013; Heays et al. 2014) are used. These data come from a concerted laboratory (e.g., Ajello et al. 1989; Helm et al. 1993; Sprengers et al. 2004; Stark et al. 2008; Lewis et al. 2008b; Heays et al. 2011) and theoretical (e.g., Spelsberg & Meyer 2001; Lewis et al. 2005b; Lewis et al. 2008c; Ndome et al. 2008) effort over the last two decades. The CO photodissociation calculation uses the new rate and self-shielding functions from Visser et al. (2009). In the CSE model from (McElroy et al. 2013), the photodissociation rates of N_2 and CO were adopted from van Dishoeck (1988), with self-shielding of CO treated only approximately (Morris & Jura 1983).

4.2.2 A new list of parent species

The identification and abundance of parent species at inner radii is the first key question to consider when modelling CSE chemistry. Typically three methods are used to constrain the parent species: TE predictions, shock-induced non-LTE predictions, and observations. The main benefit of theoretical predictions (TE and non-LTE) lies in that such models can provide a detailed list of all parent species. However, the disadvantage is that models are never as accurate as reality. Even assuming that the fundamental basis for the formation of these molecules is correct, the uncertainties in the physical processes in the inner CSE, chemical networks, and the initial abundances may still be significant. On the other hand, observationally, although high-quality data from powerful telescopes (e.g., *Herschel*, APEX, ALMA, amongst others) provide direct constraints, some species are non-detectable. For example, N_2, which is predicted to be the major elemental N reservoir in the inner layers. N_2 is symmetric and thus possesses no electric-dipole-allowed pure rotational spectrum. In addition, the identification of many species is not straightforward, due to the lack of detailed molecular data. Moreover, deduced results from spatially unresolved spectra are sometimes very model-dependent, which means considerable uncertainties also possibly exist.

Thanks to the recent progress in observations of O-rich AGB stars (e.g., Decin et al. 2010; Decin et al. 2010a,b; Kim et al. 2010; Menten et al. 2010; De Beck et al. 2013) and shock-induced non-LTE simulations (e.g., Cherchneff 2006), we are now able to employ an improved list of parent species (see Table 4.2) in this study. Wherever available, we employ

Table 4.2 — Initial fractional abundances, f_0(X) [a], of parent species, relative to H_2, for the O-rich AGB star, IK Tau.

No.	Species	f_0(X)	Comment
1	He	1.7(–1)	Solar abundance[b]
2	CO	2.0(–4)	Observation[c]
3	H_2O	6.6(–5)	Observation[d]
4	N_2	1.5(–4)	Shock-induced non-LTE abundance[e]
5	NH_3	2.0(–6)	Observation[f]
6	HCN	4.4(–7)	Observation[c]
7	CO_2	4.4(–9)	Shock-induced non-LTE abundance[e]
8	CS	8.0(–8)	Observation[c]
9	SiS	1.1(–5)	Observation[c]
10	SiO	1.6(–5)	Observation[d]
11	SO	2.0(–6)	Observation[d]
12	SO_2	2.0(–6)	Observation[c]
13	H_2S	1.0(–8)	Shock-induced non-LTE abundance[e]
14	HS	2.3(–8)	Shock-induced non-LTE abundance[g]
15	PN	3.0(–7)	Observation[h]
16	PO	9.0(–8)	Observation[h]
17	HCl	3.7(–7)	Shock-induced non-LTE abundance[e]
18	HF	7.3(–7)	TE prediction, 2[i]

[a]For species X, $f_0(X) = n(X)/n(H_2)$.
[b]Asplund et al. (2009).
[c]See Table 6 of Decin et al. (2010a).
[d]Decin et al. (2010b).
[e]Gobrecht et al. (2015).
[f]Menten et al. (2010).
[g]Gobrecht et al. (2014).
[h]De Beck et al. (2013).
[i]TE prediction, assuming elemental F has the solar abundance.

the abundance of parent species from the latest high-quality observations, otherwise those from shock-induced non-LTE abundances are adopted. Predictions from TE will only be used when no data are available from non-LTE or observational investigations. The effect of uncertainties in the abundances assumed for parent species is discussed in Sect. 4.3.12. Note that we do not simulate the chemistry in the intermediate envelope ($\lesssim$ 100 R_*) within which gas-phase chemistry may alter the abundances of parent species.

4.3 Results

4.3.1 General chemistry

Photochemistry induced by external UV photons dominates the chemistry in the expanding envelope of an AGB star. Generally, the formation and destruction processes of daughter species are controlled by the conversion XY $\rightarrow$ X $\rightarrow$ X^+, as shown in Fig. 4.3. A major finding in this work is that photoionization of molecules is also significant

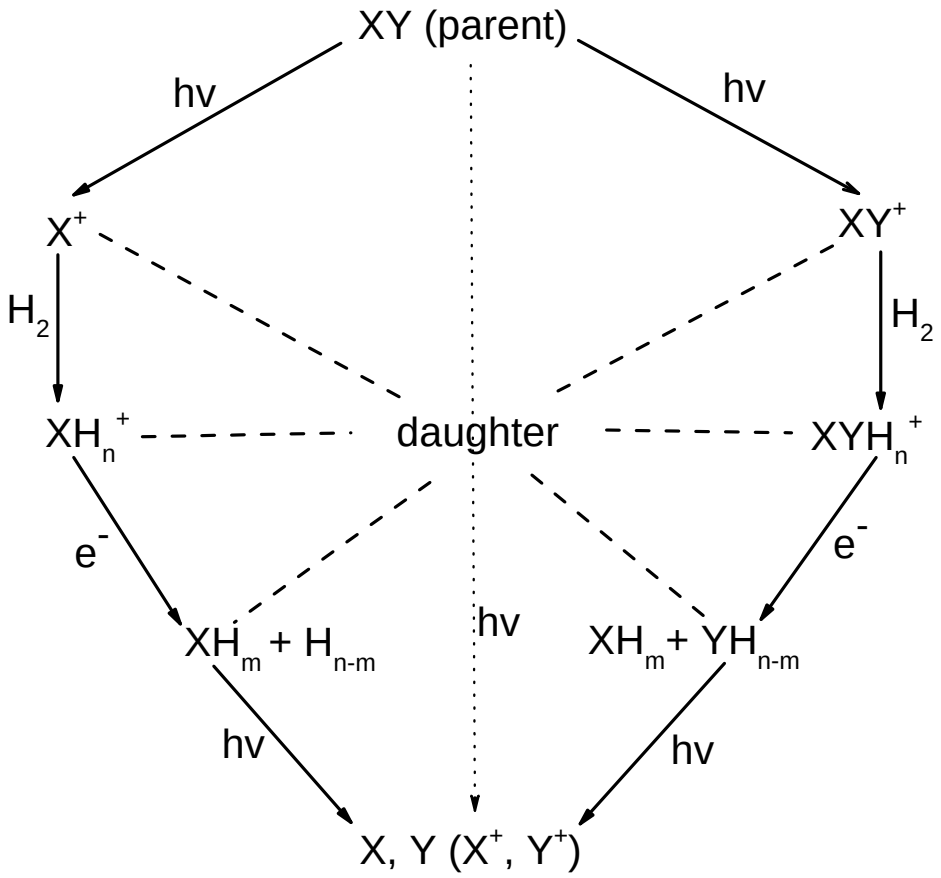

Figure 4.3 — Sketch of general pathways for parent species giving rise to daughter species in the outer CSE of an O-rich AGB star.

in the outer layers: $XY \rightarrow XY^+$. In this sense, the CSE chemistry of O-rich AGB stars differs from that found in standard photon-dominated region (PDR) models in which the ion-molecule chemistry of O-bearing species is driven by charge exchange reactions with abundant cations (see, e.g., Sternberg & Dalgarno 1995; Jansen et al. 1995a,b).

The synthesis continues with X^+ (and XY^+) abstracting H from H_2 by ion-molecule reactions forming molecular hydride cations, which is frequently followed by dissociative recombination that leads to neutral molecular hydrides, and ends up in the formation of atoms or cations at the edge of the CSE. The model predicts that negative ions are not abundant in O-rich AGB stars.

4.3.2 Impact of new N_2 and CO photodissociation rates

A proper treatment of the shielding of both N_2 and CO photodissociation has a significant impact on the chemistry in the outer CSE of AGB stars. Amongst the various shielding effects, self-shielding is the key factor in reducing the photodissociation rate of N_2 and CO (Li et al. 2014). As shown in Fig. 4.4, self-shielding of CO and N_2 becomes considerable at a large radius, around 2×10^{17} cm, where photodissociation from the external interstellar field is important. To accurately investigate the chemistry at smaller radii, we have considered full shielding (from dust, molecular H_2, atomic H, and

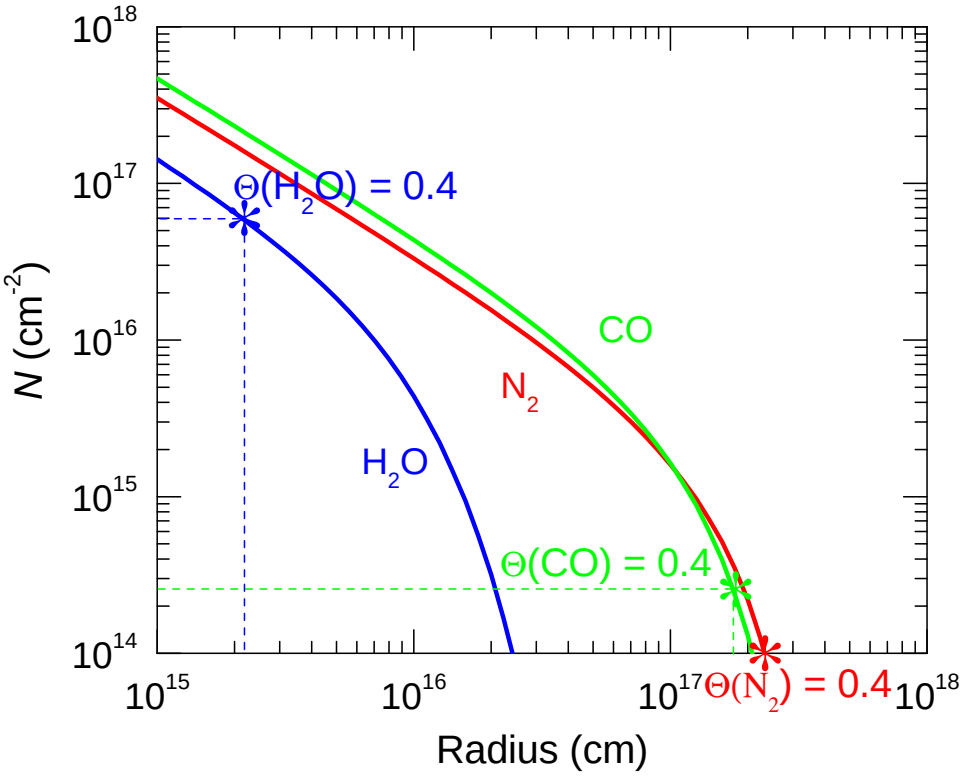

Figure 4.4 — Plot of the column densities of H_2O, CO and N_2 as a function of radius. The asterisks indicate a value of the column density that corresponds to a self-shielding factor of 0.4 for these molecules. Shielding effects become considerable when the column densities are higher than those indicated.

the molecule itself) of both N_2 and CO in all of our calculations.

Fig. 4.5 shows that the location of the transition zone from $N_2 \rightarrow$ N is shifted outwards by a factor of 7 when accurately considering shielding effects of N_2 with the SS model, whereas the location for the conversion from CO $\rightarrow C^+$ moves outwards by a factor of 2 when using updated shielding functions. These changes result in an important difference in the distributions of some daughter species whose chemistry is directly related to these species, e.g., NO and N_2H^+, as illustrated in Fig. 4.6. Other species, for instance HCN and CN, are less affected.

Another highly-abundant species, H_2O, is found to be significantly self-shielded in high abundance regions such as the planet-forming zones of circumstellar disks (Bethell & Bergin 2009). In the case of O-rich AGB stars, the self-shielding of H_2O is only considerable at radii less than 2×10^{15} cm, where the photodissociation of H_2O has not yet started to dominate its chemistry. This implies that the abundance of H_2O is too low to be self-shielded at larger radii where photodissociation becomes significant, and it is not necessary to consider self-shielding of H_2O in the CSE of AGB stars.

4.3.3 O-bearing species

The chemistry of daughter species with column densities higher than 10^{11} cm^{-2} are now discussed in different subsections based on their chemical families. To avoid repetition,

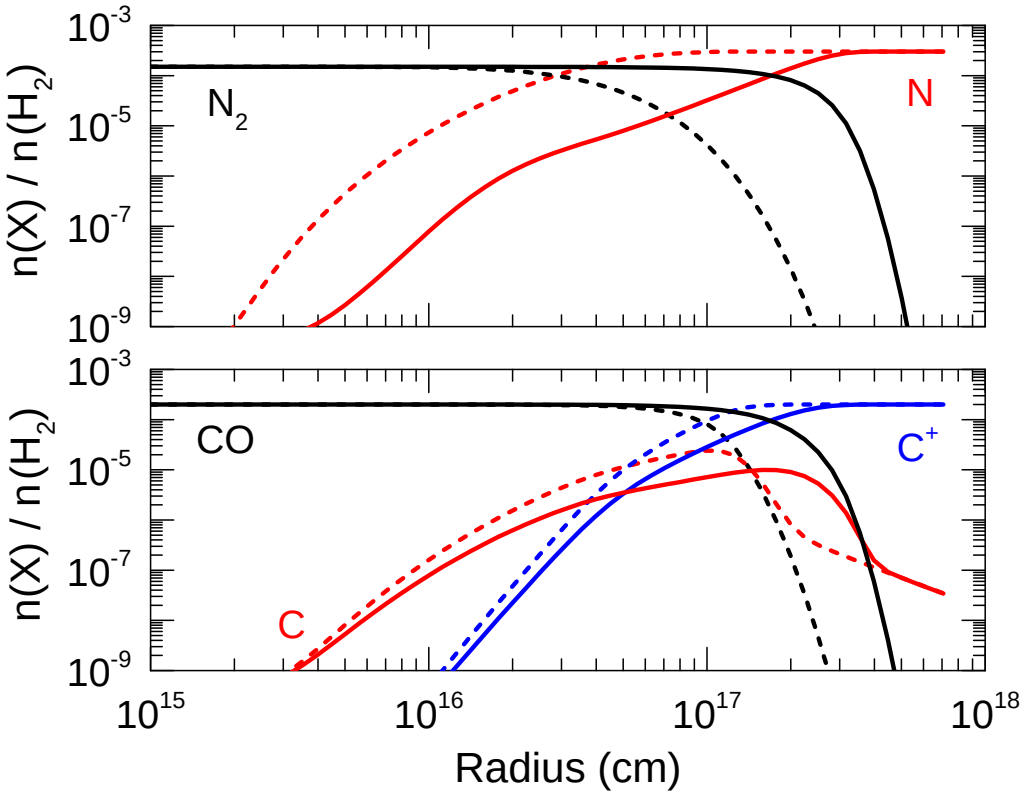

Figure 4.5 — Plot of the fractional abundances, relative to H_2, of N_2 and N (top panel), and , C^+, C, and CO (bottom panel), as a function of radius. Solid lines: from the SS model (Li et al. 2014), full shielding (dust + self- + H_2 + H) are considered using an updated N_2 photodissociation rate and self-shielding function (Li et al. 2013). Dashed lines: calculated from a model similar to that of McElroy et al. (2013) but adopting assumptions specifically for IK Tau. In this model only dust shielding is considered when calculating N_2 photodissociation, and CO self-shielding is treated only approximately.

species that can be included in multiple subsections are only discussed once. For instance, the molecule CNO, which could be discussed in the subsections of C-, O-, or N- bearing species, is only discussed in the section for N-bearing species.

The dominant chemistry for many species depends on radius, due to the large gradient in the physical conditions (i.e., visual extinction, temperatures, and gas density) in the CSEs of AGB stars. Thus, the dominating formation and destruction routes might be different in other O-rich AGB stars. In addition, different assumed abundances of parent species may lead to quite different reaction paths for the daughter species.

The most abundant O-bearing daughter species triggered by the chemistry of H_2O are OH, O_2, and H_3O^+, whose radii of peak abundances are found in the region of $(1-4)\times 10^{16}$ cm, as shown in panel (a) of Fig. 4.7. The chemistry of OH and O_2 is relatively simple, with both formed mainly via the two reactions,

$$H_2O + h\nu \rightarrow OH + H, \tag{4.2}$$
$$OH + O \rightarrow O_2 + H. \tag{4.3}$$

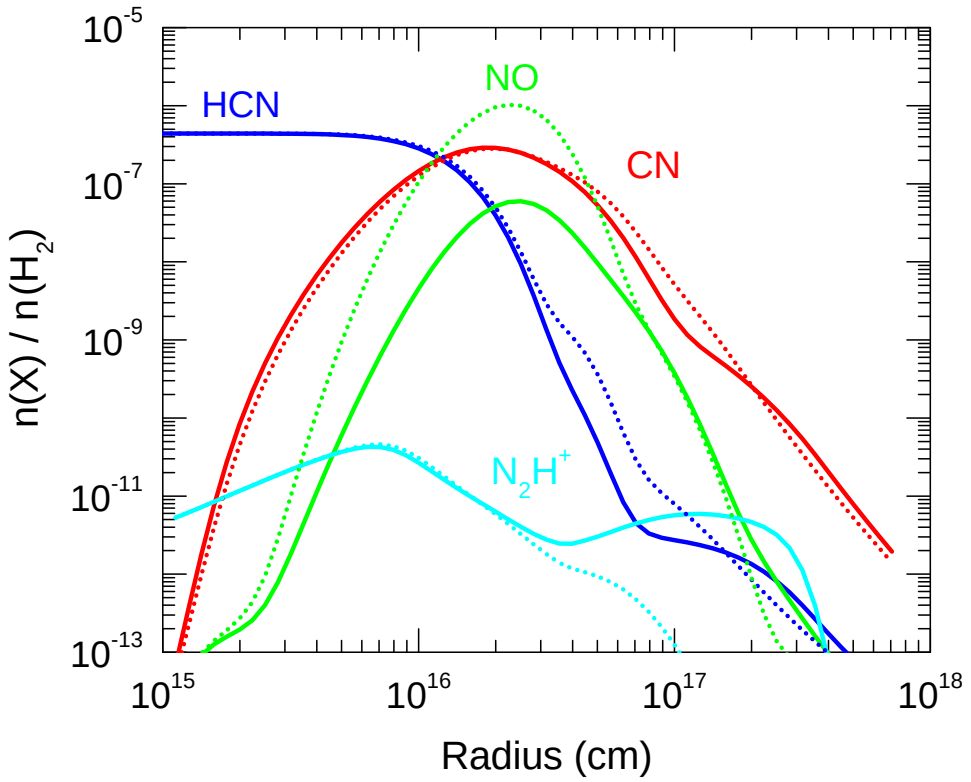

Figure 4.6 — Plot of the fractional abundances of HCN, CN, N_2H^+ and NO, relative to H_2, as a function of radius. Solid and dashed lines exhibit the results calculated from the SS model (Li et al. 2014) and that based on the updated model of McElroy et al. (2013), respectively.

H_3O^+ is mainly formed through

$$H_2O^+ + H_2 \rightarrow H_3O^+ + H, \tag{4.4}$$

where H_2O^+ comes from various routes with the relative importance depending on radius, for instance,

$$H_3^+ + O \rightarrow H_2O^+ + H, \tag{4.5}$$
$$OH^+ + H_2 \rightarrow H_2O^+ + H, \tag{4.6}$$
$$H_2O + h\nu \rightarrow H_2O^+ + e^-. \tag{4.7}$$

In the inner CSE, e.g., $\lesssim 2 \times 10^{15}$ cm, OH^+ is mainly generated by

$$He^+ + H_2O \rightarrow OH^+ + H + He, \tag{4.8}$$

where He^+ is generated by cosmic-ray ionisation. Direct OH photoionization becomes important for radii within 10^{17} cm, whilst $H_3^+ + O$ produces OH^+ at larger radii. As noted above, this is different from traditional diffuse/PDR chemistry (e.g., Gerin et al. 2010) because of the high abundance of OH here. H_3^+ is formed by the reaction between H_2 and H_2^+, where H_2^+ comes from the cosmic-ray ionization of H_2.

The destruction of most O-bearing species is dominated by photodissociation. In addition to H_2O, photodissociation of other O-bearing species, e.g., SiO, SO, CO_2, and

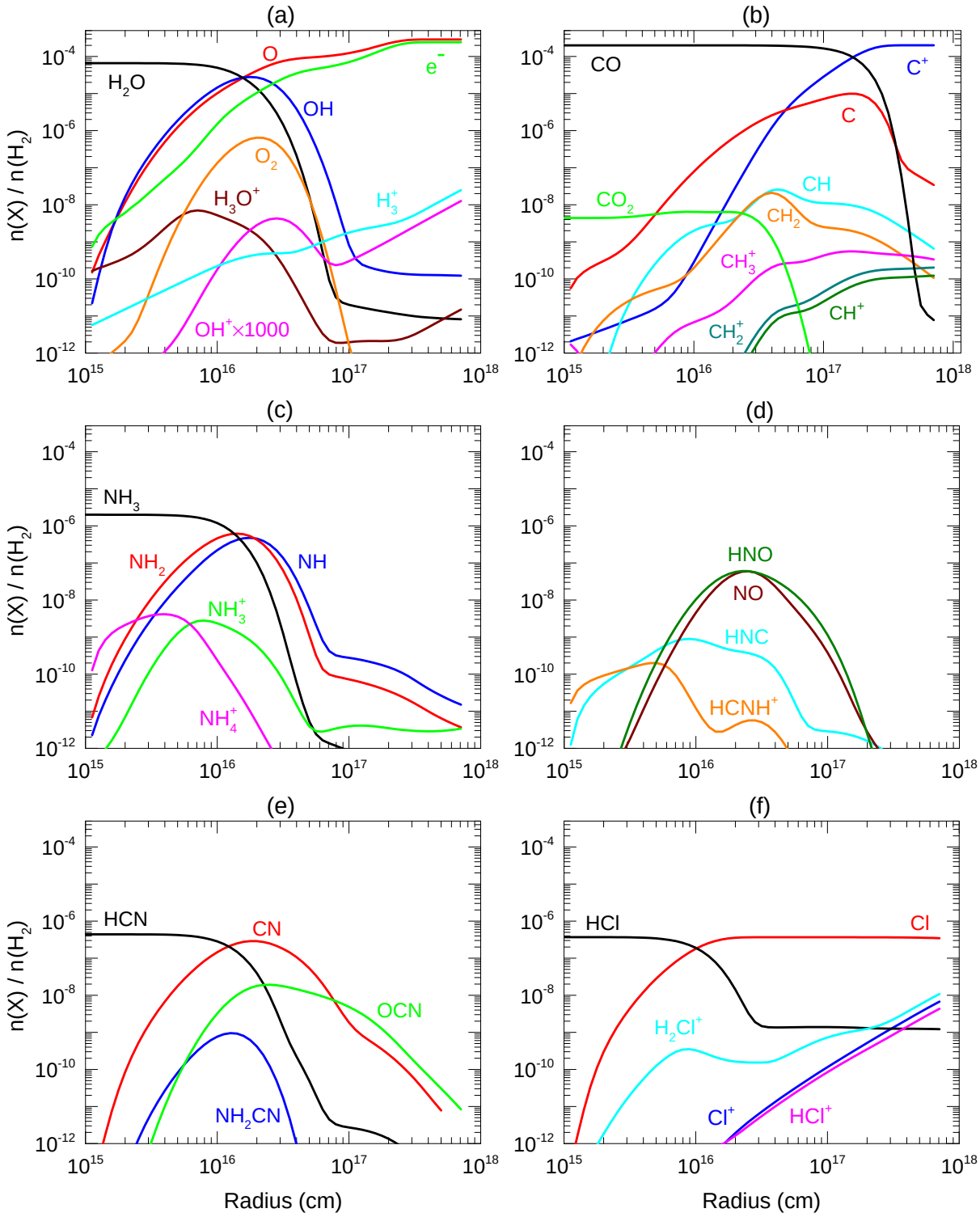

Figure 4.7 — Plot of the fractional abundances, relative to H_2, of the most abundant species in the outer CSE of the O-rich AGB star, IK Tau.

PO, amongst others, can liberate atomic oxygen at the outer edge of the CSE. CO is the key contributor at radii greater than 10^{17} cm, where A_v is less than 0.3 mag. The

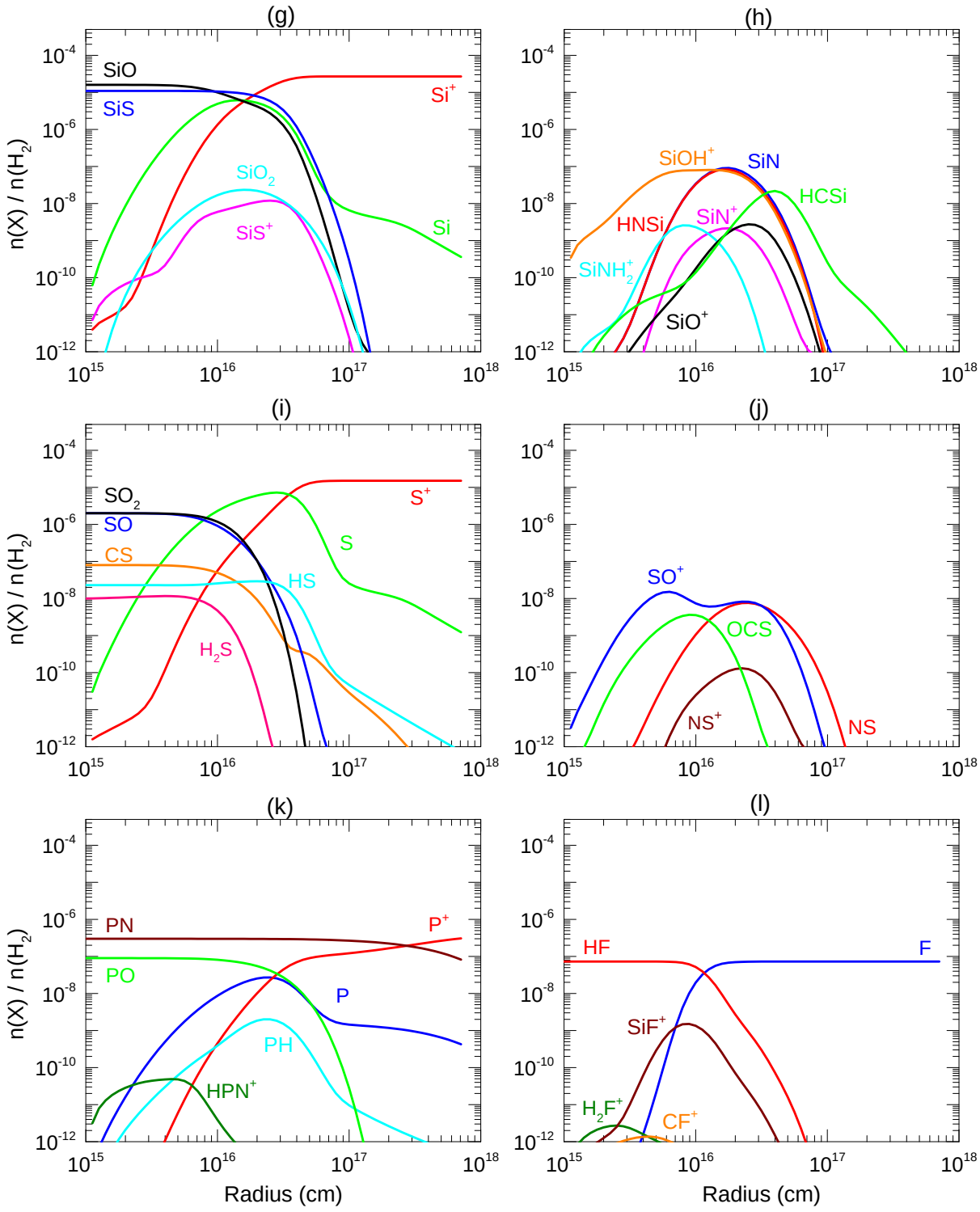

Figure 4.7 — Continued.

chemistry of CO is discussed in the following subsection. The O-bearing cations are predominantly destroyed by dissociative recombination with electrons, e.g., H_3O^+ can be

destroyed by the reaction,

$$H_3O^+ + e^- \rightarrow \text{products}. \tag{4.9}$$

The fraction of electrons is a key factor in the ion-molecule chemistry (see panel (a) of Fig. 4.7). Initially, at inner radii, e.g., $\lesssim 2 \times 10^{15}$ cm, electrons mainly arise from the cosmic-ray ionization of H_2,

$$H_2 + \text{crp} \rightarrow {H_2}^+ + e^-, \tag{4.10}$$

where crp depicts cosmic-ray particles. As the radius increases to the region where the photodissociation of H_2O becomes important, for instance, at 10^{16} cm, electrons are produced by Eq. (4.7). Further out in the CSE, e.g., 3×10^{16} cm, contributions are mainly from three channels,

$$C + h\nu \rightarrow C^+ + e^-, \tag{4.11}$$

$$S + h\nu \rightarrow S^+ + e^-, \tag{4.12}$$

$$Si + h\nu \rightarrow Si^+ + e^-. \tag{4.13}$$

At the edge of the CSE, with radius greater than 10^{17} cm, the electron density is controlled by the most abundant element, C. Further in, the electron fraction as a function of radius is significantly affected by the assumption of key parent species, especially H_2O, CO, SiS, and SiO.

4.3.4 C-bearing species

Carbon is mostly in the form of CO before it is converted into C^+ at the edge of the envelope (panel (b) of Fig. 4.7). The CO $\rightarrow$ C $\rightarrow$ C^+ conversion controls the carbon chemistry. The non-self-shielding parent species, CO_2, is less abundant and photodissociates from a radius of 3×10^{16} cm outwards. Four carbon compounds, CH, CH_2, ${CH_3}^+$, and ${CH_2}^+$ are found to be quite abundant, and are distributed at radii greater than 3×10^{16} cm, where the temperature is less than 50 K (in our model, $\sim$ 10 K, see Fig. 4.2). Therefore, their emission would only be detectable from low rotational energy levels.

The formation of CH_2 varies with radius. For instance, at 3×10^{16} cm, it is mainly formed by

$${SiCH_2}^+ + e^- \rightarrow Si + CH_2, \tag{4.14}$$

The chemistry of ${SiCH_2}^+$ is discussed in Sect. 4.3.6. At 10^{17} cm, CH_2 is mainly produced by

$${CH_3}^+ + e^- \rightarrow CH_2 + H. \tag{4.15}$$

In both cases, CH is formed through

$${CH_3}^+ + e^- \rightarrow CH + H_2, \tag{4.16}$$

whereas ${CH_3}^+$ arises from the following process at all radii,

$${CH_2}^+ + H_2 \rightarrow {CH_3}^+ + H. \tag{4.17}$$

CH_2^+ is generated through multiple channels, by

$$C^+ + H_2 \rightarrow CH_2^+ + h\nu, \tag{4.18}$$
$$CH^+ + H_2 \rightarrow CH_2^+ + H, \tag{4.19}$$

and

$$CH_2 + h\nu \rightarrow CH_2^+ + e^-. \tag{4.20}$$

In the above reactions, the majority of CH^+ is produced via the photoionization of CH, and is destroyed by Eq. (4.19) at all radii. The destruction of the neutral carbon hydrides, CH and CH_2, is dominated by photodissociation whereas that of most cations, e.g., CH_3^+, is via dissociative recombination. Interestingly, the destruction of CH_2^+ is dominated by Eq. (4.17), rather than electrons. The chemistry of four other C-bearing species, namely C_2, C_2H, CH_3OH, and HCO^+, are discussed in Sect. 4.3.12.

4.3.5 N-bearing species

The chemistry of the parent species ammonia, NH_3, controls the distribution of most N-bearing species, amongst which eight are found above the 10^{-11} abundance threshold (panel (c) of Fig. 4.7). These species are mainly located at radii between 5×10^{15} and 5×10^{16} cm from the star. The most abundant daughter species generated by NH_3 are NH_2 and NH, which have peak fractional abundances around 10^{-6}. In analogy with the corresponding oxygen and carbon species, NH_2 is produced by the photodissociation of NH_3 at radii less than its peak radius, 2.2×10^{16} cm, whereas dissociative recombination of NH_3^+ with e^- dominates at greater radii. NH is the product of the photodissociation of NH_3 and NH_2 throughout the entire CSE, but with a significant contribution from the reaction between NH_3^+ and e^- when the radius is greater than 1×10^{17} cm.

The relatively abundant cation, NH_3^+, is mainly formed through the photoionization of NH_3 for radii inside its peak abundance, and by the reaction between NH_2^+ and H_2 at greater radii. NH_2^+ comes from the photoionization of NH_2 and reactions between NH^+ and H_2. The chemistry of NH_4^+ is less complex, and forms mainly via the reaction between NH_3^+ and H_2. Only at very inner radii, e.g., 2×10^{15} cm, is it formed by the reaction of NH_3 and H_3O^+.

The chemistry of NH_3 also gives rise to other N-bearing species, such as HNO, NO, HNC and $HCNH^+$ (panel (d) of Fig. 4.7) at radii between $10^{16} - 10^{17}$ cm. First, the breaking down of NH_3 generates NH_2, which reacts with atomic O and produces HNO. Then, HNO is photodissociated to NO. The formation channels of NO vary with radius, e.g., a non-negligible amount of NO is formed from the reaction between N and OH in the inner regions $\leq 2 \times 10^{15}$ cm, and by OCN + O at radii greater than 5×10^{17} cm.

Throughout the CSE, HNC is mainly produced via $HCNH^+$, in the following two reactions

$$HCNH^+ + NH_3 \rightarrow HNC + NH_4^+, \tag{4.21}$$

and

$$HCNH^+ + e^- \rightarrow HNC + H. \tag{4.22}$$

The formation of $HCNH^+$ is complex. At radii less than 10^{16} cm, it is mainly formed via the reaction between H_3O^+ and HCN. However, at larger radii, it is entirely formed via

$$HCN^+ + H_2 \rightarrow HCNH^+ + H, \tag{4.23}$$

where HCN^+ is the product of reactions between $C^+ + NH_2$, and $CN^+ + H_2$. CN^+ comes from the reaction between C^+ and NH. Therefore, HCN contributes most to the formation of HNC in the inner regions whereas NH_3 plays the most important role in the outer regions.

Another important N-bearing parent species, HCN, controls the chemistry of CN, OCN, and NH_2CN (panel (e) of Fig. 4.7). In our model, HCN starts to photodissociate at a radius of 10^{16} cm, breaking down into its daughter species, CN. Note that there are other routes leading to the formation of CN at its peak radius, i.e., the photodissociation of HNC, and the reaction between OCN and H. Its destruction at large radii is simply dominated by photodissociation.

The species OCN is mainly formed via

$$OH + CN \rightarrow OCN + H \tag{4.24}$$

at radii less than 8×10^{16} cm, whereas dissociative recombination dominates its formation at greater radii, via

$$HNCO^+ + e^- \rightarrow OCN + H \tag{4.25}$$

and

$$HOCN^+ + e^- \rightarrow OCN + H \tag{4.26}$$

with assumed-equal reaction rate constants, $1.5 \times 10^{-7}\,cm^3\,s^{-1}$. However, $HNCO^+$ and $HOCN^+$ are totally formed by the reaction between OCN and $H_3{}^+$ (with a reaction rate constant of $1.6 \times 10^{-8}\,cm^3\,s^{-1}$) and so comprise a cyclic formation pathway and not the dominant route to OCN bond formation. The rates for the above reactions are adopted from Quan et al. (2010), where more detailed discussions about these species can be found.

The chemistry of NH_2CN is dependent on both NH_3 and HCN. This species is simply formed by the following reaction,

$$NH_3 + CN \rightarrow NH_2CN + H. \tag{4.27}$$

and destroyed by photodissociation,

$$NH_2CN + h\nu \rightarrow NH_2 + CN. \tag{4.28}$$

4.3.6 Si-bearing species

The photodissociation/photoionization processes of parent species, SiO/SiS $\rightarrow$ Si $\rightarrow$ Si^+, control the silicon chemistry and gives rise to other Si-bearing species (panels (g) and (h) of Fig. 4.7). Similar to N-bearing species, most silicon compounds have peak abundances for radii between 10^{16} and 10^{17} cm. In total, seven high-abundance daughter molecules are found: SiS^+, SiO_2, $SiOH^+$, SiN, HNSi, SiN^+ and $SiNH_2{}^+$.

In the inner layers, at radii smaller than 2×10^{16} cm, the abundance of Si is higher than Si^+ and its formation is dominated by the photodissociation of SiO. As the distance from the star increases, Si is photoionized to form Si^+, and therefore contributes to the electron density. SiS^+ comes from SiS, via charge exchange

$$SiS + S^+ \rightarrow SiS^+ + S, \tag{4.29}$$

around its peak radius, and by the reaction between C^+ and SiS in other regions. Its destruction is dominated by

$$SiS^+ + e^- \rightarrow Si + S. \tag{4.30}$$

The presence of OH at a high abundance ($\sim 10^{-5}$) generates a significant abundance of $SiOH^+$ in an O-rich CSE,

$$Si^+ + OH \rightarrow SiO^+ + H, \tag{4.31}$$
$$SiO^+ + H_2 \rightarrow SiOH^+, \tag{4.32}$$

which is destroyed by dissociative recombination in the outer layers,

$$SiOH^+ + e^- \rightarrow Si + OH, \tag{4.33}$$
$$SiOH^+ + e^- \rightarrow SiO + H. \tag{4.34}$$

Reactions (4.31) and (4.32) dominate the formation and destruction of SiO^+. Similarly, the parent species NH_3 generates NH, then increases the abundance of SiN^+, which is formed and destroyed via the following processes at all radii

$$NH + Si^+ \rightarrow SiN^+ + H, \tag{4.35}$$
$$SiN^+ + e^- \rightarrow Si + N. \tag{4.36}$$

$SiNH_2{}^+$ is formed and destroyed in a very similar way, via

$$NH_3 + Si^+ \rightarrow SiNH_2{}^+ + H, \tag{4.37}$$
$$SiNH_2{}^+ + e^- \rightarrow SiN + H_2, \tag{4.38}$$
$$SiNH_2{}^+ + e^- \rightarrow HNSi + H. \tag{4.39}$$

The chemistry of SiO_2 is triggered by SiO, via the following reaction throughout the envelope,

$$SiO + OH \rightarrow SiO_2 + H. \tag{4.40}$$

SiN is mainly generated by Eq. (4.38) within 10^{16} cm, but from the photodissociation of HNSi at greater radii. At all radii, HNSi is produced by Eq. (4.39). The destruction of all of these neutral silicon compounds is dominated by photodissociation, although their actual rates are quite uncertain and are experimentally difficult to measure.

The species HCSi peaks at a relatively larger radius, 4×10^{16} cm, arising from SiS, through

$$\mathrm{SiS} + \mathrm{C}^+ \rightarrow \mathrm{SiC}^+ + \mathrm{S}, \tag{4.41}$$
$$\mathrm{SiC}^+ + \mathrm{H_2} \rightarrow \mathrm{HCSi}^+ + \mathrm{H}, \tag{4.42}$$
$$\mathrm{HCSi}^+ + \mathrm{H_2} \rightarrow \mathrm{SiCH_2}^+ + \mathrm{H}, \tag{4.43}$$

and

$$\mathrm{SiCH_2}^+ + \mathrm{e}^- \rightarrow \mathrm{HCSi} + \mathrm{H}, \tag{4.44}$$

and is dissociated by UV photons.

4.3.7 S-bearing species

The conversion from the parents $\mathrm{SO_2/SO/SiS} \rightarrow \mathrm{S} \rightarrow \mathrm{S}^+$ in the CSE is the key to the sulphur chemistry (panels (i) and (j) of Fig. 4.7). The increase in atomic S is caused by the photodissociation of SO and $\mathrm{SO_2}$ (first releasing SO then S) at radii less than 10^{16} cm, with a contribution from the breaking down of SiS at larger radii, $\geq 3 \times 10^{16}$ cm. Beyond this point, S is converted into S^+ by photoionization. The less abundant parent species, $\mathrm{H_2S}$ and HS, play a less important role in the chemical network.

In total, we find four abundant daughter species. At all radii, OCS is formed via

$$\mathrm{CS} + \mathrm{OH} \rightarrow \mathrm{OCS} + \mathrm{H}, \tag{4.45}$$

and NS is formed via

$$\mathrm{NH} + \mathrm{S} \rightarrow \mathrm{NS} + \mathrm{H}. \tag{4.46}$$

Similar to other neutral species, the destruction of OCS and NS is dominated by photodissociation. NS^+ has a relatively low abundance, coming from NH reacting with S^+. Like most cations, it is destroyed by dissociative recombination. SO^+ is produced by the following two reactions,

$$\mathrm{SO} + \mathrm{h}\nu \rightarrow \mathrm{SO}^+ + \mathrm{e}^-, \tag{4.47}$$
$$\mathrm{OH} + \mathrm{S}^+ \rightarrow \mathrm{SO}^+ + \mathrm{H}, \tag{4.48}$$

and, again, is destroyed by dissociative recombination.

4.3.8 P-bearing species

PN and PO are the two phosphorus-bearing parent species in our model. The conversion process $\mathrm{PN/PO} \rightarrow \mathrm{P} \rightarrow \mathrm{P}^+$, which is dominated by the photodissociation and photoionization, controls the the phosphorus chemistry (panel (h) in Fig. 4.7). Our model produces a significant and likely unrealistic abundance of PN at very large radii where all other molecular species have been destroyed by the interstellar radiation field. This is due to the neglect of PN photoionisation in the Rate12 reaction network despite the low ionisation threshold of this molecule (Wu & Fehlner 1975) and a photoabsorption cross section that is likely to be comparable to that of electronically-similar CO and $\mathrm{N_2}$.

Two species, HPN^+ and PN, are found to be abundant. HPN^+ is mainly formed via

$$H_3O^+ + PN \rightarrow HPN^+ + H_2O, \tag{4.49}$$

and destroyed by three channels assumed to have equal branching ratios,

$$HPN^+ + e^- \rightarrow PH + N, \tag{4.50}$$
$$HPN^+ + e^- \rightarrow P + NH, \tag{4.51}$$
$$HPN^+ + e^- \rightarrow PN + H. \tag{4.52}$$

PH arises from Eq. (4.50) at radii smaller than 1×10^{16} cm. Contribution from the routes

$$H_2O + P^+ \rightarrow HPO^+ + H, \tag{4.53}$$
$$HPO^+ + e^- \rightarrow PH + O, \tag{4.54}$$

becomes most important as the radius increases. Its destruction is dominated by photodissociation.

4.3.9 Cl-bearing species

The chemistry of Cl-bearing species is initiated by the photodissociation of the parent species, HCl (panel (f) of Fig. 4.7). The most abundant Cl-bearing daughter molecule in this model is H_2Cl^+. The breakdown of HCl leads to two species,

$$HCl + h\nu \rightarrow Cl + H, \tag{4.55}$$
$$HCl + h\nu \rightarrow HCl^+ + e^-, \tag{4.56}$$

At all radii, ∼90% of HCl goes to Eq. (4.55) whereas ∼10% goes to Eq. (4.56). H_2Cl^+ is formed via

$$HCl^+ + H_2 \rightarrow H_2Cl^+ + H. \tag{4.57}$$

and destroyed by

$$H_2Cl^+ + e^- \rightarrow Cl + H_2. \tag{4.58}$$

The cation, Cl^+, arises from the photoionization of Cl. It is worth mentioning that H_2Cl^+, HCl^+, and H_2O^+ have been detected by the *H*erschel space observatory in the diffuse interstellar medium (e.g. Gerin et al. 2010; Lis et al. 2010; De Luca et al. 2012; Neufeld et al. 2012; Gerin et al. 2013). Another Cl-bearing species, NaCl, has been found in IK Tau with an abundance of 4×10^{-9} (Milam et al. 2007). Unfortunately we don't have the chemistry of Na-bearing species in our network, thereby an extension of the chemical network would be useful for a further understanding of the chlorine chemistry. Our model shows that the abundance of CCl^+ is negligible and is not shown in the plot.

4.3.10 F-bearing species

This is the first time that F-chemistry is included in a CSE model of an O-rich AGB star. The photodissociation of the parent species, HF, liberates atomic F and gives rise to other F-bearing species (panel (l) of Fig. 4.7). Three daughter species, SiF^+, CF^+, and H_2F^+ are found to be most abundant. In particular, SiF^+ has not been detected in the ISM due to the the depleted elemental abundance of silicon. However, we predict that it may be detectable in IK Tau at a radius of $(2-4)\times10^{16}$ cm. At all radii, SiF^+ and CF^+ are formed by the reactions,

$$HF + Si^+ \rightarrow SiF^+ + H, \tag{4.59}$$
$$HF + C^+ \rightarrow CF^+ + H, \tag{4.60}$$

and are destroyed by

$$SiF^+ + e^- \rightarrow Si + F, \tag{4.61}$$
$$CF^+ + e^- \rightarrow C + F. \tag{4.62}$$

H_2F^+ is formed via two routes,

$$HF + {H_3}^+ \rightarrow H_2F^+ + H_2, \tag{4.63}$$
$$HF^+ + H_2 \rightarrow H_2F^+ + H, \tag{4.64}$$

where HF^+ arises from

$$He^+ + HF \rightarrow F^+ + He + H, \tag{4.65}$$

and

$$F^+ + H_2 \rightarrow HF^+ + H. \tag{4.66}$$

The destruction of H_2F^+ is dominated by

$$H_2F^+ + e^- \rightarrow F + H_2, \tag{4.67}$$

and

$$H_2F^+ + e^- \rightarrow HF + H. \tag{4.68}$$

4.3.11 Comparison with observations

The calculated fractional abundances, peak radii, and total column densities of the top 36 daughter species in IK Tau are presented in Table 4.3. Observational information is only available for CN and HCO^+. For CN, the calculated peak abundance, total column density, and peak radius are in good agreement with the observations from Kim et al. (2010) and Decin et al. (2010a). For HCO^+, the calculated peak radius is in excellent agreement with the observations of Pulliam et al. (2011), but the fractional abundance and total column density are orders-of-magnitude lower than the observations. This will be discussed in the following section. The calculated total column densities of a few parent

Table 4.3 — Calculated total column densities, peak abundances (relative to H_2), and peak radii of the daughter molecules in the CSE of the O-rich AGB star, IK Tau.

No.	Species	$N_{\rm total}$ ($\rm cm^{-2}$)	Peak abundance	Peak radius (cm)
1	OH	5.4(15)	2.8(–5)	1.8(16)
2	C	4.0(14)	9.9(–6)	1.6(17)
3	NH_2	1.4(14)	6.2(–7)	1.4(16)
4	NH	8.2(13)	4.8(–7)	1.8(16)
5	O_2	7.8(13)	6.5(–7)	2.0(16)
6	CN	5.8(13)	2.9(–7)[a]	1.8(16)
7	$SiOH^+$	4.0(13)	8.1(–8)	1.3(16)
8	SiN	1.3(13)	9.1(–8)	1.8(16)
9	HNSi	1.2(13)	8.2(–8)	1.6(16)
10	HNO	7.9(12)	6.1(–8)	2.2(16)
11	SO^+	6.6(12)	1.5(–8)	6.3(15)
12	NO	5.9(12)	6.0(–8)	2.5(16)
13	SiO_2	5.9(12)	2.4(–8)	1.6(16)
14	NH_4^+	3.7(12)	4.1(–9)	4.0(15)
15	SiC	3.3(12)	6.7(–8)	4.5(16)
16	H_3O^+	3.0(12)	7.1(–9)	7.1(15)
17	OCN	2.7(12)	1.9(–8)	2.5(16)
18	SiS^+	2.4(12)	1.2(–8)	2.5(16)
19	CH	2.0(12)	2.6(–8)	4.5(16)
20	CH_2	1.2(12)	2.1(–8)	4.0(16)
21	HCSi	1.1(12)	2.2(–8)	4.0(16)
22	OCS	1.1(12)	3.6(–9)	8.9(15)
23	NS	9.1(11)	7.6(–9)	2.5(16)
24	NH_3^+	8.9(11)	2.8(–9)	7.9(15)
25	$SiNH_2^+$	6.5(11)	2.6(–9)	7.9(15)
26	HNC	3.9(11)	8.9(–10)	8.9(15)
27	SiF^+	3.3(11)	1.5(–9)	8.9(15)
28	SiN^+	3.2(11)	2.2(–9)	1.8(16)
29	PH	2.7(11)	2.0(–9)	2.5(16)
30	H_3^+	2.5(11)	2.5(–8)	7.1(17)
31	SiO^+	2.5(11)	2.7(–9)	2.5(16)
32	C_2	2.3(11)	7.6(–9)	6.3(16)
33	NH_2CN	1.9(11)	9.5(–10)	1.3(16)
34	$HCNH^+$	1.8(11)	2.0(–10)	5.0(15)
35	H_2Cl^+	1.7(11)	1.1(–8)	7.1(17)
36	HCO^+	1.6(11)[b]	4.0(–10)[c]	2.5(16)[c]

[a]Observationally, Decin et al. (2010a) obtained 2(-10) − 6(-8), whereas Kim et al. (2010) deduced two values, 5.1(-8) or 1.6(-7), corresponding to two cases where two different radii of CN were assumed in their models.

[b]Observationally, Edwards et al. deduced 1.0(13) $\rm cm^{-2}$ (Priv. Comm.)

[c]Observationally, Pulliam et al. (2011) obtained a peak abundance of 4.4(-8) at radius 3.9(16) cm.

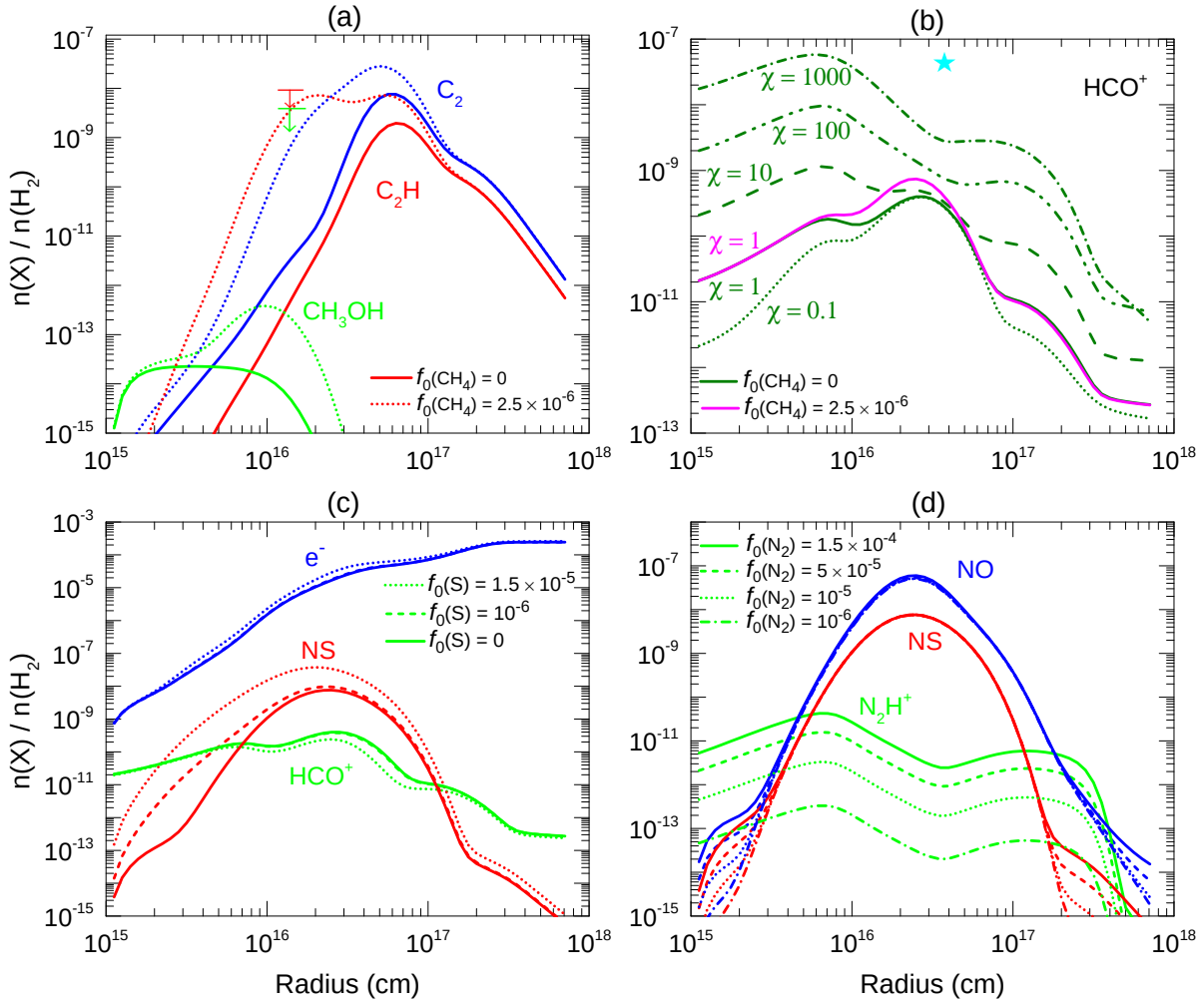

Figure 4.8 — Plot of the fractional abundances of some daughter species as a function of radius, calculated using different initial fractions of CH_4 (panels a and b), atomic S (panel c), and N_2 (panel d), in addition to various cosmic-ray rates. In panel (a): the arrows depict the upper limits of C_2H (red) and CH_3OH (green) deduced in the observational work of Marvel (2005), where the peak radii of these species was assumed to be 1.5×10^{16} cm. In panel (b): χ is the scaling factor of the cosmic-ray ionisation rate and the star indicates the observational result from Pulliam et al. (2011).

species, such as HCN, CS, SiS, SiO, SO, and SO_2, are also compared to the observational results (Kim et al. 2010). Agreements are within a factor of 10 demonstrating that the parent species' abundances are not altered significantly by gas-phase chemistry *en route* through the inner region of the outer envelope. However, note that we have neglected gas-phase chemical processing through the intermediate envelope which may also affect the parent species' abundances. A thorough comparison with observations requires calculations of the excitation and radiative transfer to compute line intensities rather than column densities, which is beyond the scope of the present work.

4.3.12 Sensitivities to the initial abundances

The assumed abundance of parent species is of particular importance for the predicted distribution and abundance of daughter species. The identification and abundance of most of these species at inner radii can be well constrained by both observations and theoretical models. However, the initial abundances of some parent species, e.g., N_2, remain unclear. In addition, there is some discussion in the literature concerning the presence of additional species, e.g., atomic S and CH_4, in the inner envelope with non-negligible abundances (see, e.g., Willacy & Millar 1997; Cherchneff 2006). A possible solution for inferring the presence and abundance of these species is via a few relevant daughter species.

Methane (CH_4) is not assumed to be a parent species in the current study, based on the conclusions from the observational work of Marvel (2005), where the upper limits on abundances for C_2H and CH_3OH (methanol) were deduced to be 9.7×10^{-9} and 4.5×10^{-9}, respectively. Gobrecht et al. (2014) also find that CH_4 is not formed efficiently via gas-phase chemistry in the inner wind ($r \lesssim 10R_*$) in their model of IK Tau. Our model results are in general agreement with these conclusions. In the earlier photochemical model of Willacy & Millar (1997), CH_4 was assumed to be a parent molecule with a large fractional abundance, 3.0×10^{-5}, to explain the chemistry of a few carbon species, especially the unexpected presence of HCN in O-rich envelopes. At that time HCN was thought to be a daughter species and formed via reactions between atomic N, CH_2 and CH_3, which are photoproducts of N_2 and CH_4. The presence of CH_4 as a parent also significantly increases the fractions of both C_2H and CH_3OH, by which one can constrain the upper limits for methane.

We find that the maximum abundance of CH_4 in the O-rich AGB star, IK Tau, is 2.5×10^{-6}, in order to be consistent with the observed upper limit for the C_2H abundance, see panel (a) of Fig. 4.8. Regardless of including or excluding CH_4 as a parent molecule in the model, the predicted CH_3OH is at least 5 orders of magnitude lower than its observational upper limit, peaking at radii between $10^{15} - 10^{16}$ cm. One of the most important channels for CH_3OH formation is via

$$CH_3^+ + H_2O \rightarrow CH_3OH_2^+ + h\nu, \tag{4.69}$$
$$CH_3OH_2^+ + e^- \rightarrow CH_3OH + H, \tag{4.70}$$

where the chemistry of CH_3^+ is discussed in Sect. 4.3.4. Note that in dense interstellar clouds, CH_3OH is mainly formed on grain surfaces (Watanabe & Kouchi 2002; Garrod & Herbst 2006; Geppert et al. 2006; Fuchs et al. 2009) which is neglected here, however, the physical conditions in the CSE are not amenable to ice formation. Typically, ices exist in regions where $A_v > 1$ which corresponds to the high temperature region (> 600 K) in our model of IK Tau, see Fig. 4.2. Nevertheless, our results for gas-phase methanol are well within the observed upper limit from Marvel (2005).

At the radii where C_2 possesses its peak abundance, it mainly arises from

$$C^+ + SiC \rightarrow Si^+ + C_2. \tag{4.71}$$

C_2H can be formed via multiple channels, amongst which the following routes contribute

most,

$$\mathrm{C_2} + \mathrm{h}\nu \rightarrow \mathrm{C_2}^+ + \mathrm{e}^-, \tag{4.72}$$
$$\mathrm{C_2}^+ + \mathrm{H_2} \rightarrow \mathrm{C_2H}^+ + \mathrm{H}, \tag{4.73}$$
$$\mathrm{C_2H}^+ + \mathrm{H_2} \rightarrow \mathrm{C_2H_2}^+ + \mathrm{H}, \tag{4.74}$$
$$\mathrm{C_2H_2}^+ + \mathrm{e}^- \rightarrow \mathrm{C_2H} + \mathrm{H}. \tag{4.75}$$

HCO^+ has been detected in IK Tau, with an abundance of 4.4×10^{-8} at a radius of 3.9×10^{16} cm (Pulliam et al. 2011). The current model gives a peak radius that is in excellent agreement with this observation, but produces a lower abundance of HCO^+. This is the case even where the cosmic-ray ionisation rate of $\mathrm{H_2}$ is increased with respect to its standard value in our models of $1.2 \times 10^{17}\,\mathrm{s}^{-1}$ by a scaling factor, χ, up to a value of $\times 1000$. The inclusion of the maximum amount of $\mathrm{CH_4}$ consistent with observations, 2.5×10^{-6}, only increases HCO^+ by a minor amount, see panel (b) of Fig. 4.8. Another model assuming a higher abundance for the initial CO only slightly enhances the peak abundance of HCO^+. At the radius of its peak abundance, i.e., 3×10^{16} cm, HCO^+ is mainly formed from C^+ with CO^+ and HOC^+ as intermediates via the reactions

$$\mathrm{C}^+ + \mathrm{OH} \rightarrow \mathrm{CO}^+ + \mathrm{H}, \tag{4.76}$$
$$\mathrm{CO}^+ + \mathrm{H_2} \rightarrow \mathrm{HOC}^+ + \mathrm{H}, \tag{4.77}$$
$$\mathrm{CO}^+ + \mathrm{H_2} \rightarrow \mathrm{HCO}^+ + \mathrm{H}, \tag{4.78}$$
$$\mathrm{C}^+ + \mathrm{H_2O} \rightarrow \mathrm{HOC}^+ + \mathrm{H}, \tag{4.79}$$
$$\tag{4.80}$$

and

$$\mathrm{HOC}^+ + \mathrm{H_2} \rightarrow \mathrm{HCO}^+ + \mathrm{H_2}. \tag{4.81}$$

Only a minor amount (10%) of HCO^+ is formed by the reaction between C^+ and $\mathrm{H_2O}$. If the abundance of parent species in our model photodissociating to form C^+ is increased then a minor enhancement of HCO^+ results. The destruction of HCO^+ at its peak location is controlled only by the reaction

$$\mathrm{HCO}^+ + \mathrm{e}^- \rightarrow \mathrm{CO} + \mathrm{H}. \tag{4.82}$$

The peak abundance of HCO^+ may also be enhanced by the inclusion of the neutral analogue, HCO, as a parent species. A potential route to HCO in the inner CSE is via the reaction between H and CO with a third body (see, e.g., Baulch et al. 2005). The backwards reaction has a large energy barrier (≈ 8000 K Baulch et al. 2005); hence, potentially leading to appreciable abundances of HCO. The inclusion of HCO formation and destruction in models of the inner CSE of O-rich AGB stars are worth investigating in the future.

The electron abundance, which has been discussed in Sect. 4.3.3, is the most significant factor in destroying many cations. The C-, S-, and Si-bearing parent species contribute most to the formation of electrons, depending on the radius. However, the abundances of

C and Si related species are strongly constrained as discussed in Sect. 4.2.2 and here we only explore the effect of the uncertainty introduced by the unknown amount of atomic S amongst the parent species.

In our fiducial model we exclude atomic S as a parent species. However, the shock-induced non-LTE simulation of Cherchneff (2006) suggested that most elemental S is in atomic form for O-rich AGB stars, which was further confirmed in the latest simulations specifically focussing on IK Tau (Cherchneff, Priv. Comm.). Since the solar abundance of elemental S relative to H_2 is 2.6×10^{-5} (Asplund et al. 2009), and we have 1.1×10^{-5} in SiS in our model (see Table 4.2), we assume the maximum amount of S in the inner CSE to be 1.5×10^{-5}. As can be seen in panel (c) of Fig. 4.8, the uncertainty of including or excluding atomic S has a minor effect on the total abundance of electrons, and therefore on HCO^+. Interestingly, NS is found to be sensitive to the initial abundance of atomic S, and may be useful as a diagnostic measurement. More interestingly, as can be seen in panel (d) of Fig. 4.8, both NS and NO are hardly affected by the initial N_2 abundance. It is hard to detect N_2 directly, but it can be indirectly constrained by the abundance of N_2H^+, which is mainly formed via the reaction

$$N_2 + H_3{}^+ \rightarrow N_2H^+ + H_2. \tag{4.83}$$

At larger radii, e.g., 10^{17} cm, its formation is dominated by

$$N_2 + He^+ \rightarrow N_2{}^+ + He, \tag{4.84}$$

$$N_2{}^+ + H_2 \rightarrow N_2H^+ + H, \tag{4.85}$$

where the He^+ is generated by cosmic-ray ionization. In all situations, the abundance of N_2H^+ is directly related to the initial abundance of N_2, but this species has not yet been detected in the CSEs of AGB stars.

4.4 Concluding remarks

We simulated the chemistry in O-rich circumstellar envelopes of AGB stars. We have calculated radial abundances suitable for guiding future observational studies and identified the most abundant species. Our model includes the latest gas-phase reaction network and photodissociation processes, including a spectroscopically realistic treatment of N_2 and CO self-shielding. The H_2O column is found to be too low to self shield. With the proper self-shielding factors, the $N \rightarrow N_2$ and $C^+ \rightarrow CO$ transitions are shifted outward by factors of 7 and 2, respectively, in the fiducial model representing IK Tau. We also adopt a selection of precursor parent species based on observations and the latest non-LTE model of the interior CSE of IK Tau.

There are few quantitative observational constraints on the molecular abundances in IK Tau but based on our experience with the C-rich CSE surrounding IRC +10216 (Li et al. 2014) we expect order-of-magnitude accuracy for our predictions of C-, N-, O-, and Si-bearing molecules. The reaction networks for less-abundant elements (S, P, Cl, and F) are not as well known but significant abundances of their host molecules are predicted by our model. Many molecules have peak abundance between 10^{16} to 10^{17} cm from the star where the ionisation and dissociation of parent species provides a source

of radicals but where molecules are still somewhat shielded from interstellar radiation. Key steps in the intervening chemistry are hydrogen abstraction of radical ions with H_2 and the production of neutral fragments by dissociative recombination and the ultimate destruction of all molecules by the ISRF.

We find chemical links between potentially-observable daughter molecules and the abundances of parent species in the inner CSE. Observationally-derived upper limits for the amount of C_2H and CH in IK Tau provide a low constraint on the relative abundance of the potential parent CH_4, $< 2.5 \times 10^{-6}$. We also find that observations of NS and N_2H^+ could provide indirect constraints on the parent abundances of atomic S and N_2.

Our modelled molecular abundances are also sensitive to the assumed physical parameters of the CSE. We find that the stellar mass-loss rate, which is usually not straightforward to obtain from observations, has a large impact on the calculated abundances. On the other hand, variations in the envelope expansion velocity and cosmic-ray ionisation rate are not as significant (see the Appendix).

Many of the predictions of our models (both overall abundances and peak abundance radii) can be tested directly by spatially resolved observations with ALMA in the near future.

Acknowledgements

X. Li thanks TJM for his hospitality during a two-week visit to Queen's University Belfast (QUB) in 2014, and thanks Profs. Xander Tielens and Leen Decin for some stimulating discussion. X. Li also would like to thank Drs. Jessica Edwards and Robin Pulliam for the discussion on HCO^+ in IK Tau.

Astrochemistry in Leiden is supported by the Netherlands Research School for Astronomy (NOVA), by a Spinoza grant and grant 648.000.002 from the Netherlands Organisation for Scientific Research (NWO), and by the European Community's Seventh Framework Programme FP7/2007-2013 under grant agreements 291141 (CHEMPLAN) and 238258 (LASSIE). Astrophysics at QUB is supported by a grant from the STFC. C. W. acknowledges support from NWO (program number 639.041.335).

4.5 Appendix: An extended investigation of the CSE species

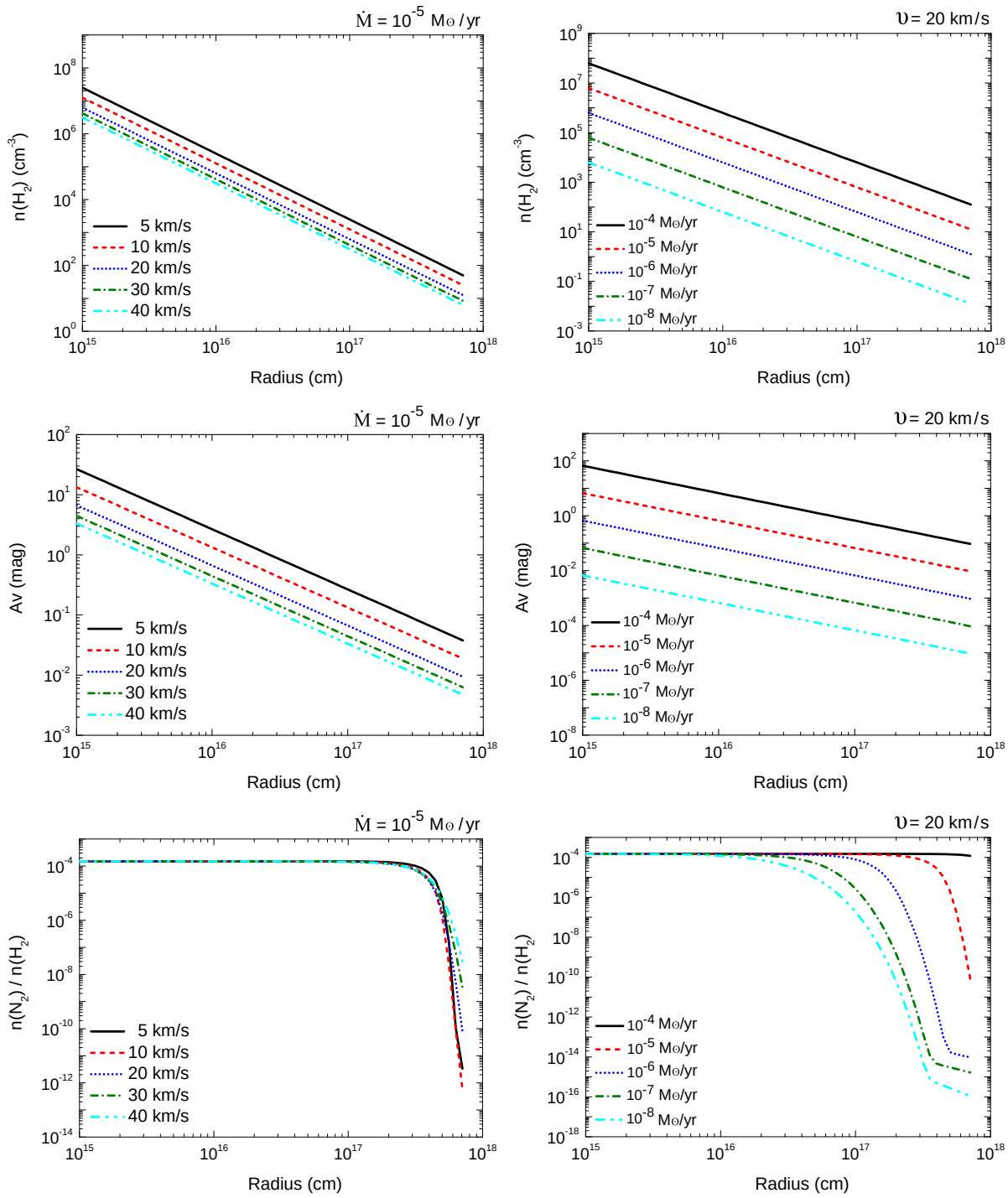

Figure 4.1 — Effects of envelope expansion velocity and mass-loss rate on gas density, visual extinction, and distributions of species in the outer layers of O-rich AGB stars, part A.

The chemical evolution of molecular species in an expanding CSE naturally depends on the physical structure of the AGB star and its envelope. In particular, the mass-loss

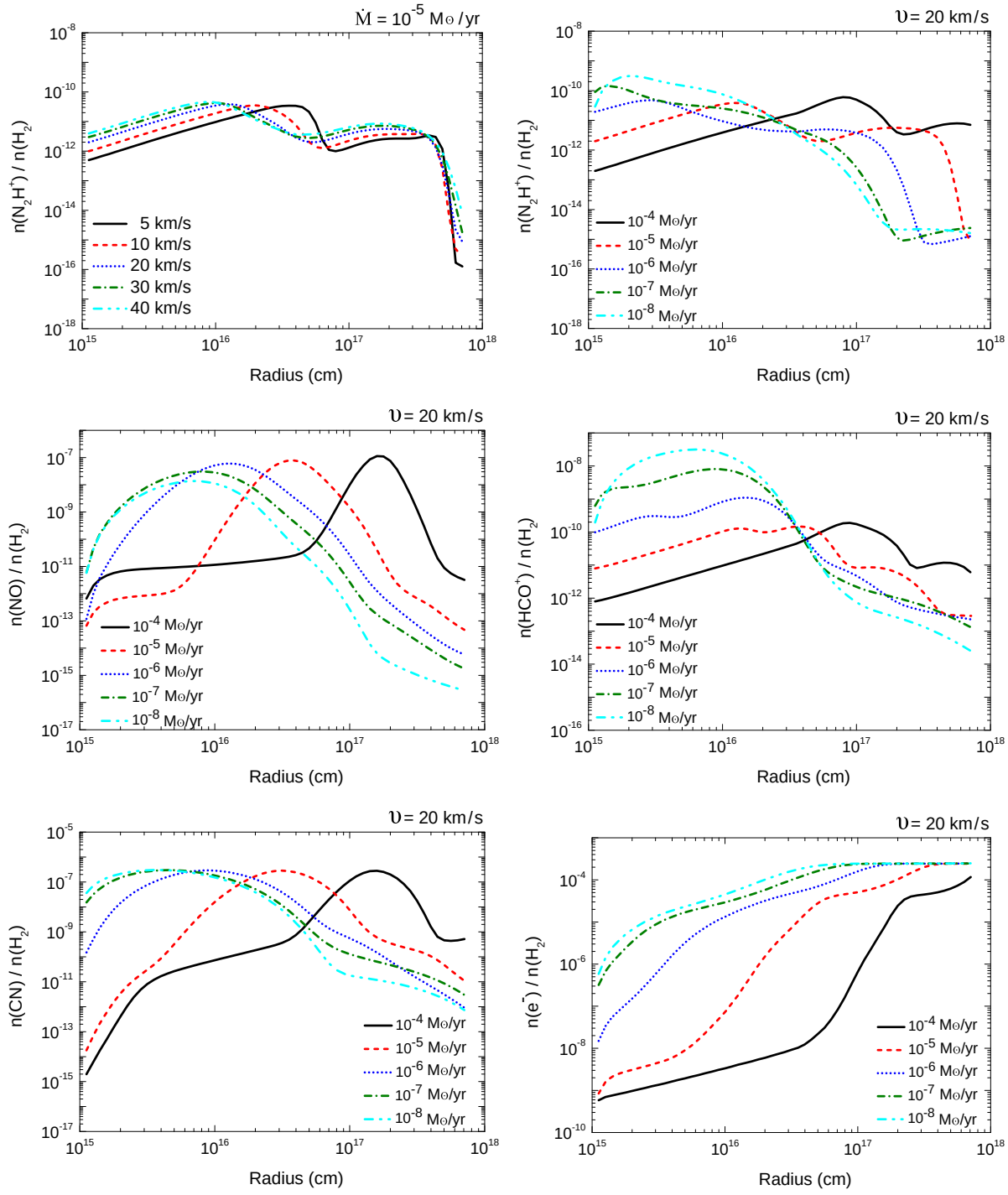

Figure 4.1 — Continued, part B.

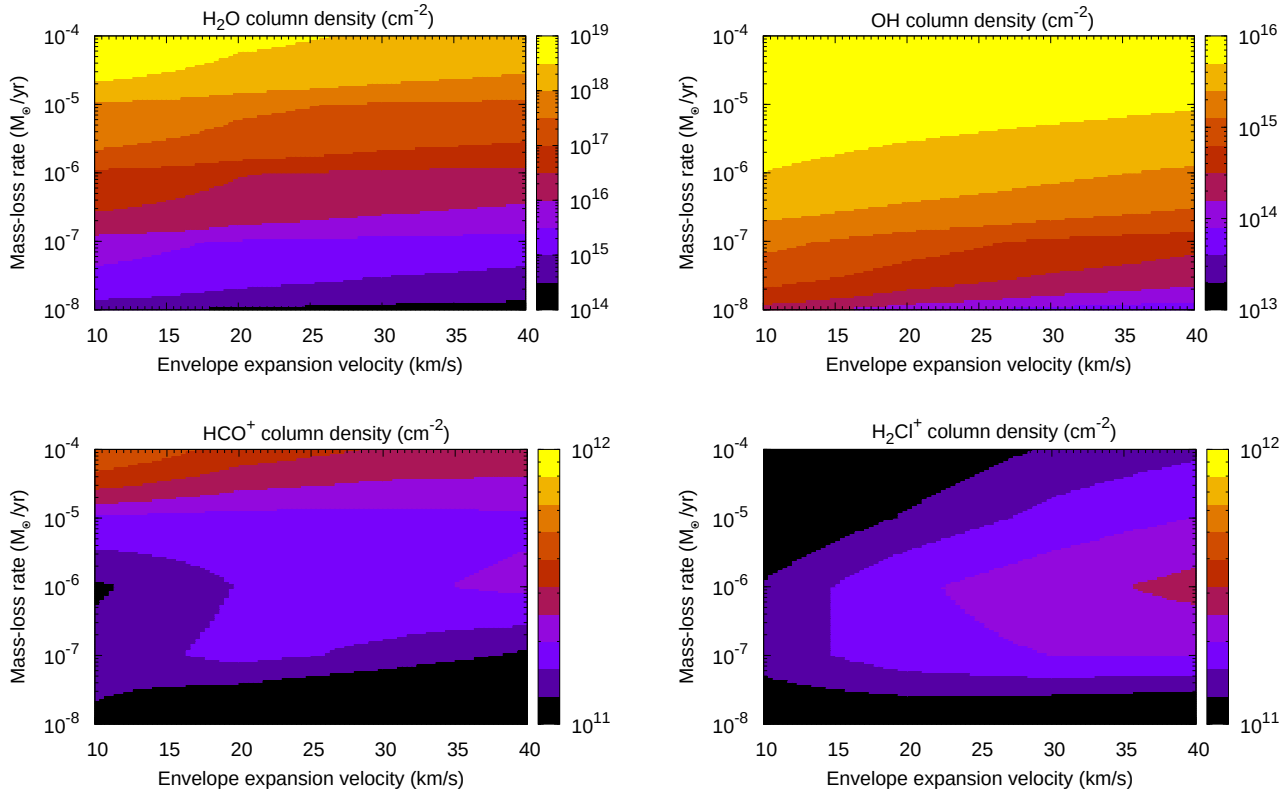

Figure 4.2 — Total column densities for a sample of species in the CSE of O-rich AGB stars, as a function of mass-loss rate and envelope expansion velocity.

rate plays an important role in the distribution of the molecules in the outer envelope, but large uncertainties always exist in its measurement. Starting from our physico-chemical model of IK Tau, we explore here the chemistry of a few interesting species over a range of typical mass-loss rates and gas expansion velocities, $10^{-8} - 10^{-4}$ $M_\odot$ yr^{-1} (Kwon & Suh 2012) and $5 - 40$ km s^{-1}, respectively. The predicted trends are relevant to O-rich AGB stars in general.

The effect of altering the mass-loss rate of an AGB star on gas density, visual extinction, and the abundance of molecular species (both parent and daughter) is studied assuming a fixed envelope expansion velocity, 20 km s^{-1}, whereas the dependence on expansion velocity is studied by assuming a fixed mass-loss rate of 10^{-5} $M_\odot$ yr^{-1}. Fig. 4.5.1 shows that stars possessing a large mass-loss rate can drive the gas to greater distances, whereas the peak abundances of most neutral species, e.g., CN, NO, are less affected. This implies that peak radii of daughter species retrieved from observations may give information about the mass-loss rate. In contrast, the peak abundances of cations, e.g., N_2H^+ and HCO^+, are decreased and the peak radius moves outwards with increasing mass-loss rate. Note that the decrease in peak abundance is more apparent for HCO^+ than N_2H^+ and for the highest mass-loss rate, 10^{-4} $M_\odot$ yr^{-1}, the peak abundance for the latter begins to increase as the peak is pushed outwards. This effect on cations is due to the physical structure of the CSE and not to their enhanced chemical destruction. This is, their destruction is dominated by dissociative recombination with electrons and the

electron density decreases significantly with increasing mass loss.

Total column densities of four molecular species are shown in Fig. 4.5.2 as functions of mass-loss rate and gas expansion velocity. This figure, together with the upper left panel of Fig. A.1, shows that the dependence of the chemistry on the expansion velocity is negligible within usual observational uncertainties. Trends for all parent species are similar to those plotted for H_2O, whose column density increases with increasing mass-loss rate. However, the modelled column density trends for daughter species are quite variable, e.g., the behaviour of OH is similar to that of its parent species H_2O, whereas H_2Cl^+ exhibits a quite different trend. According to this study, the upper-limit of the HCO^+ column density in O-rich envelope is 5×10^{11} cm^{-2}.